Continental Shelf Research 213 (2021) 104299

Contents lists available at ScienceDirect

Continental Shelf Research

journal homepage: www.elsevier.com/locate/csr

Research papers

Rapid reduction of tidal amplitude due to form drag in a narrow channel

Rachel M. Horwitz [a,*], Stephanne Taylor [a], Youyu Lu [a], Jean-Philippe Paquin [b], Douglas Schillinger [a], David A. Greenberg [a]

[a] Bedford Institute of Oceanography, Fisheries and Oceans Canada, 1 Challenger Drive, Dartmouth, Nova Scotia, Canada
[b] Canadian Centre for Meteorological and Environmental Prediction, Environment and Climate Change Canada, Dorval, Quebec, Canada

ARTICLE INFO

Keywords:
Form drag
Tides
River
Estuary
Bay of Fundy

ABSTRACT

Reversing Falls is a large sill in a narrow section of the Saint John River on the northern coast of the Bay of Fundy, Canada. Reversing Falls limits tides from propagating farther up the river and impedes river water flowing seaward. This work aims to describe the physical processes that control flow over Reversing Falls by using output from a regional numerical model. We find form drag is more important than frictional drag for limiting the M2 tide propagation over Reversing Falls. Despite large tides and strong stratification suggestive of estuarine processes, the dynamics at Reversing Falls are dominated by a steady balance between drag and the surface pressure gradient, with the distinction that all terms in this river-like dynamical balance change sign on a semi-diurnal tidal cycle.

1. Introduction

Reversing Falls is the largest sill in a narrow channel linking Saint John Harbour to the complicated river and lake system of the Saint John River in New Brunswick, Canada (Fig. 1a). Saint John Harbour is on the northern coast of the Bay of Fundy, and there is an 8 m tidal range in the harbour (Trites, 1960). As the tides propagate from harbour to river, a series of sills spanning the lowest 5 km of the river drastically reduces the amplitude of the tide to just a 0.5 m range above Reversing Falls (Trites, 1960; Metcalfe et al., 1976; Godin, 1991). In the spring and fall, the Saint John River also carries significant runoff with a spring peak around 3000 m^3 s^{-1}. Depending on the river stage and tide phase, the Reversing Falls channel can be fully fresh, full ocean salinity, or have a 0 to 32 salinity stratification over the 20 m water column (Trites, 1960; Metcalfe et al., 1976; Church, 2014).

Typically, as ocean tides enter shallow inlets, bottom friction slows the flow and dissipates energy, causing the amplitude of the primary tidal constituent to decrease and the phase to lag as the tide propagates up the estuary. The water depth dependence of shallow water wave speed, quadratic bottom stress, and nonlinear advection produce higher harmonics when tides propagate into shallow water (e.g. Prandle, 1991; Parker, 1991). These higher harmonics are responsible for the asymmetry between ebb and flood durations common in estuaries (Speer and Aubrey, 1985; Friedrichs and Aubrey, 1988), including Saint John. Strong river flow further damps upstream tidal propagation (Godin, 1985, 1991) and adds to the ebb–flood asymmetry of frictional effects.

On a flat or gradually varying seabed, bottom friction causes the drag that slows a flow; when flow passes over a steep obstacle, an additional force, called form drag, opposes the flow. Form drag results from high and low bottom pressure anomalies that develop on the upstream and downstream slopes of the obstacle, respectively [e.g. Kundu, 2012, p. 387; Pratt and Whitehead, 2008, p. 69]. These pressure anomalies can be induced by flow separation at the boundary or by changes in stratification from internal waves, eddies, and mixing. Form drag has been shown to be larger than frictional drag, and a first order term in the momentum balance, in locations with steep bathymetry underlying coastal tidal oscillations (MacCready et al., 2003; Edwards et al., 2004; Warner and MacCready, 2009; Warner et al., 2013), shelf currents (Moum and Nash, 2000; Nash and Moum, 2001), and the large scale Antarctic Circumpolar Current (Johnson and Bryden, 1989; Gille, 1995).

Most of the M2 constituent from Saint John Harbour is blocked from propagating beyond Reversing Falls, but a small amplitude M2 tide propagates 90 km into the Saint John River system (Metcalfe et al., 1976). Above the falls, the fortnightly and monthly variations in water level are larger than the amplitudes of the driving frequencies. As explained by Godin (1991), these low frequency variations are not induced by the small tidal oscillations above the falls, but rather caused by variation in the tidal range coming from the harbour: large spring tides limit river flow from passing over the falls so the water accumulates upstream until smaller neap tides allow it to pass downstream.

* Corresponding author.
E-mail address: Rachel.Horwitz@dfo-mpo.gc.ca (R.M. Horwitz).

https://doi.org/10.1016/j.csr.2020.104299
Received 21 November 2019; Received in revised form 28 August 2020; Accepted 10 November 2020
Available online 13 November 2020

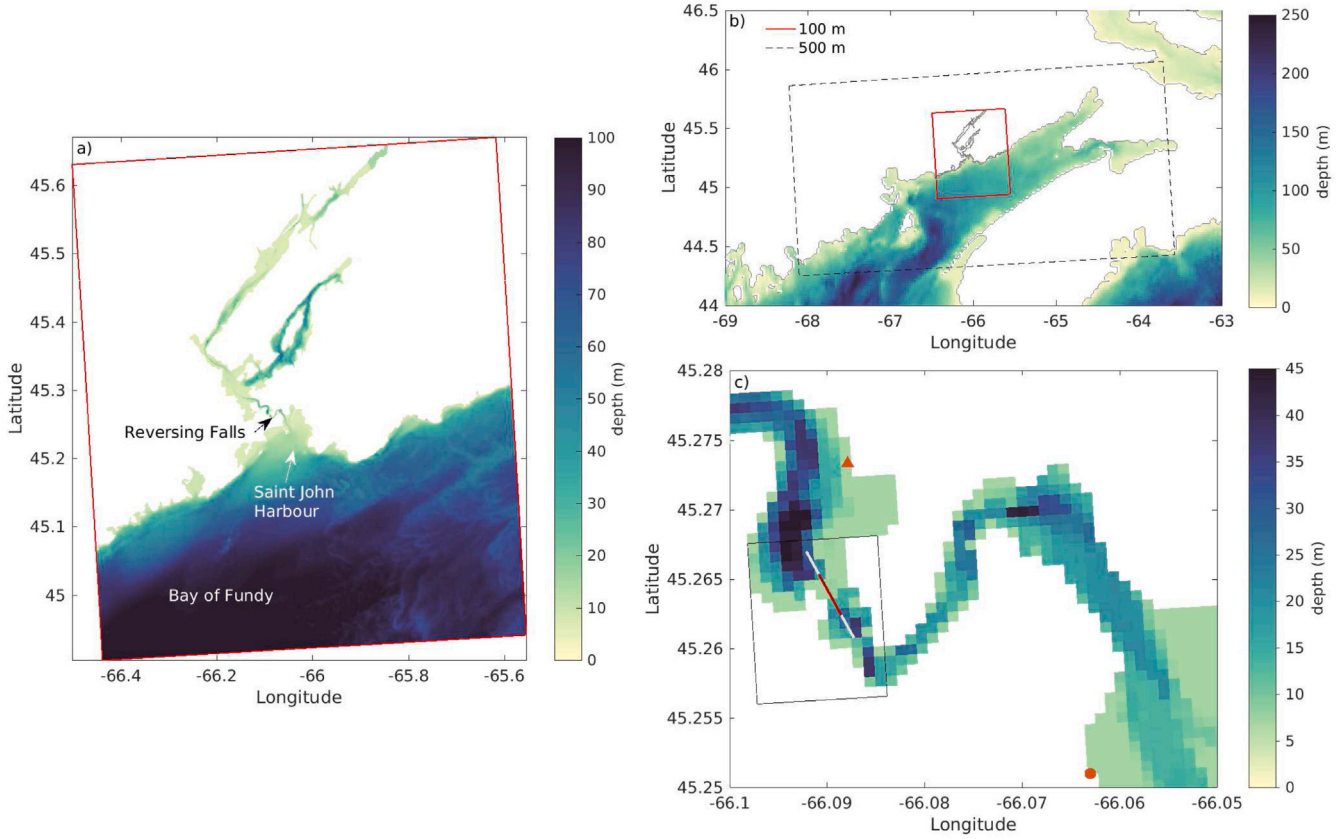

Fig. 1. (a) Bathymetry of SJAP100, 100 m resolution domain; (b) Boundaries of 1-way nested 500 m (black dashed) and 100 m (red) resolution sub-domains, shown on partial map of the 1/36° model bathymetry; (c) SJAP100 bathymetry in Reversing Falls region with line indicating orientation of 1st principal coordinate of velocities from black boxed region. Segment used for momentum calculations highlighted in red. ECCC (triangle) and CHS (filled circle) tide gauge locations indicated in orange. (For interpretation of the references to colour in this figure legend, the reader is referred to the web version of this article.)

Reversing Falls is named for the rapids and whirlpools that appear in the lee of the sill on both ebb and flood tides. Bottom friction is certainly larger on the shallow sill than in the deeper basins on either side, but the drastic damping of the M2 tide and large fraction of the channel cross section obstructed by the falls suggest that form drag plays an important dynamical role as well. Two previous works have simulated the barotropic (Sankaranarayanan and McCay, 2003) and baroclinic (Leys, 2007) flows over Reversing Falls, but neither explored the dynamics of the process. Through empirical tuning of bed roughness and cross-sectional area over Reversing Falls, Leys (2007) determined that river discharge was extremely sensitive to cross-sectional area and insensitive to bed roughness, and concluded that Reversing Falls is a hydraulic control point. Currents in Saint John Harbour are driven by the combination of large tides and outflow from the Saint John River, so understanding the effect of Reversing Falls on the outflow is necessary to accurately model and predict the harbour currents as well as the tidal influence on the upstream river flooding that periodically inundates riverside communities.

In this work, we aim to quantify the form and frictional drag contributions that control the tidal and mean flow in the lower Saint John River. This work utilizes a regional numerical model that has been demonstrated to capture the tidal and residual circulation around Saint John Harbour (Paquin et al., 2019) and presents the opportunity to assess the cause of the drastic reduction of tidal amplitude in the lower Saint John River estuary. The remainder of this manuscript is organized as follows. Section 2 provides the derivation of the relevant momentum terms, including form drag. Section 3.1 describes the numerical model. Section 3.2 describes the tidal propagation over Reversing Falls. Section 3.3 compares the strength of form drag to frictional drag. Section 3.4 characterizes the dominant momentum balance over Reversing Falls. Section 4 presents a discussion and Section 5 summarizes the results.

2. Form drag derivation

Flow over a bathymetric obstacle usually causes higher pressure on the upstream face and lower pressure on the downstream face. Form drag is the net force that arises from the normal forces that balance the pressure anomalies on the surface of an obstacle (Fig. 2). The pressure difference can be due to surface height anomalies or differences in stratification. Form drag is the result of energy loss rather than the cause, and it is one way that the energy loss feeds back to slow the flow.

Form drag appears in the volume-integral of the Boussinesq momentum equations. We follow MacCready et al.'s (2003) derivation of the along-channel (or flow-aligned) momentum equation. We assume no rotation, as the channel of interest is much narrower than either the internal or external deformation radii. Using Gauss's Theorem to convert several terms from volume integrals to surface area integrals yields

$$\int_V \frac{\partial u}{\partial t} dV + \int_A u u_n dA = -\int_A \frac{p'}{\rho_o} \hat{\mathbf{i}} \cdot \hat{\mathbf{n}} dA + \int_A \nu \frac{\partial u}{\partial n} dA \quad (1)$$

where surface area A has faces with normal direction $\hat{\mathbf{n}}$, which bound volume, V (Fig. 2a); $\hat{\mathbf{i}}$ is the unit vector in the along-channel direction; u is the along-channel velocity, u_n is the component of u normal to the surfaces denoted by A; pressure $p = p_o(z,t) + p'(x,y,z,t)$ and density $\rho = \rho_o + \bar{\rho}(z,t) + \rho'(x,y,z,t)$, with $\partial p_o/\partial z = -g(\rho_o + \bar{\rho})$ and $\partial p'/\partial z = -g\rho'$.

The pressure anomaly term of (1) can be divided into integrals over the bottom, top, and side surface areas: A_{bot}, A_{top}, and A_{sides}. The form

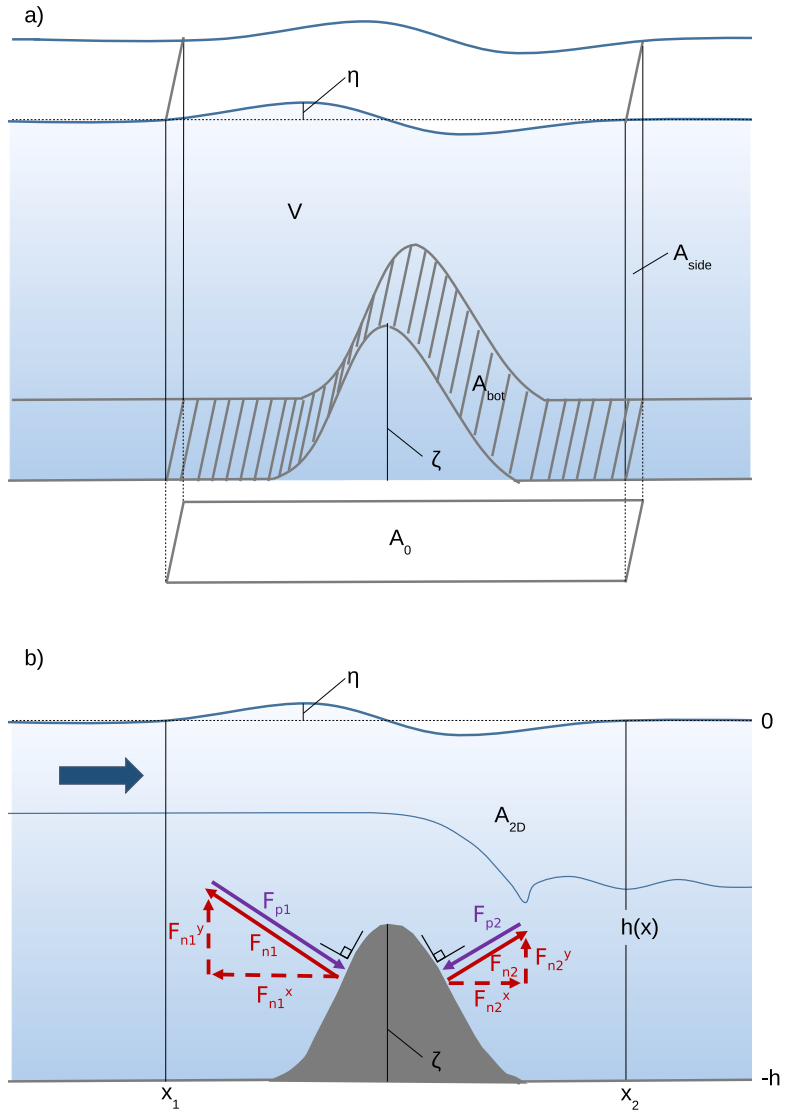

Fig. 2. (a) Schematic diagram of flow over a three-dimensional obstacle with labelled variables described in Section 2. (b) Two-dimensional version of schematic, with arrows indicating force balance that leads to form drag. If the force from pressure on the upstream face, F_{p1}, is larger than F_{p2}, then F^x_{n1}, the horizontal component of the normal force required to balance the pressure force, will be larger than F^x_{n2}, so a net horizontal force will oppose the flow.

drag, D_{form}, is the integral of the pressure anomaly over A_{bot}.

$$D_{\text{form}} \equiv -\int_{A_{\text{bot}}} \frac{p'}{\rho_o}\hat{\mathbf{i}}\cdot\hat{\mathbf{n}}dA = -\int_{A_o} \frac{p'_b}{\rho_o}\frac{\partial\zeta}{\partial x}dA \tag{2}$$

where A_o is the projected horizontal area of the bottom surface A_{bot}, p'_b is the bottom pressure anomaly, and ζ is the bathymetry height. p'_b can be further divided into contributions from surface height variation, η, and density anomalies, ρ'. We do not consider atmospheric pressure anomalies because they vary over horizontal scales much larger than the region examined in this study, so $p' = 0$ at the surface and therefore A_{top} does not contribute to the surface area integral. The pressure anomalies on A_{sides} generate barotropic and baroclinic pressure gradients.

Assuming no cross-channel variation and no sea surface stress, the two-dimensional (Fig. 2b) version of the momentum equation becomes

$$\underset{[1]}{\int_{A_{2D}} \frac{\partial u}{\partial t}dA} + \underset{[2]}{\left(\int_{-h}^{\eta} u^2 dz\right)\Big|_{x_1}^{x_2}} = \underset{[3]}{-\left(\int_{-h}^{\eta}\frac{p'}{\rho_o}dz\right)\Big|_{x_1}^{x_2}} \underset{[4]}{-\int_{x_1}^{x_2} g\eta\frac{\partial\zeta}{\partial x}dx} \underset{[5]}{-\int_{x_1}^{x_2}\left(\int_{-h}^{\eta}\frac{\rho' g}{\rho_o}dz\right)\frac{\partial\zeta}{\partial x}dx} \underset{[6]}{-\int_{x_1}^{x_2}\frac{\tau^b}{\rho_o}dx} \tag{3}$$

where A_{2D} is a two-dimensional projection of the three-dimensional integral volume; η is the sea surface elevation; h is the bathymetric depth; and x_1 and x_2 are the along-channel endpoints of integration, chosen to have the same bathymetric depth. On the left side of (3) are the [1] acceleration and [2] advection terms. On the right hand side are [3] pressure gradient, [4] external form drag, D_{ext}, [5] internal form drag, D_{int}, and [6] frictional drag, D_{frc}, terms.

Term [3] of (3) can be further divided into barotropic and baroclinic components

$$\underset{[3]}{-\left(\int_{-h}^{\eta}\frac{p'}{\rho_o}dz\right)\Big|_{x_1}^{x_2}} = \underset{[3a]}{-gH\eta\Big|_{x_1}^{x_2}} \underset{[3b]}{-\left(\int_{-h}^{\eta}\int_{z}^{\eta}\frac{\rho' g}{\rho_o}dzdz\right)\Big|_{x_1}^{x_2}} \tag{4}$$

with total water depth $H = h + \eta$.

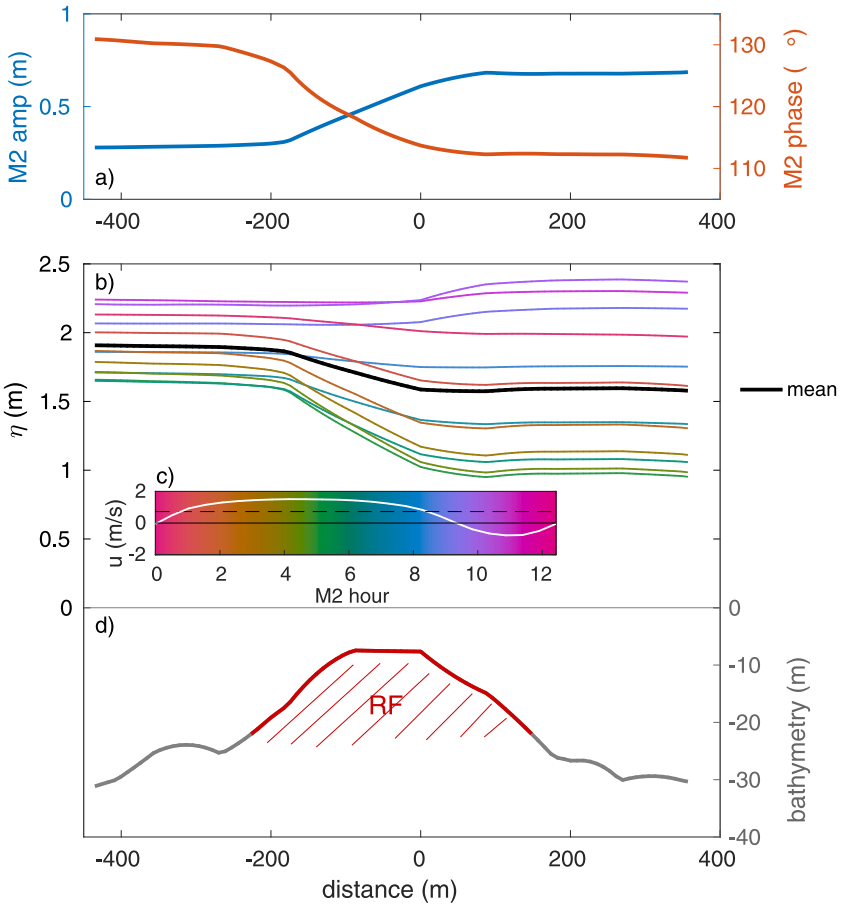

Fig. 3. (a) Along-channel sections of M2 amplitude and phase relative to GMT. (b) Mean (black) and M2 phase-averaged sea surface height. Phase is referenced to 2016/04/01 00:00:00 and averaged over $\pi/12$ rad increments. Lines shown every $\pi/6$ rad. Colorbar lists equivalent hour in 12.42 h cycle; (c) Phase-average of segment-mean along-channel velocity (white), and the mean velocity of 0.73 m s^{-1} for reference (black dashed), sharing the x-axis with the colorbar for (b); (d) Channel bathymetry with segment used for momentum calculations highlighted in red. (For interpretation of the references to colour in this figure legend, the reader is referred to the web version of this article.)

3. Model analysis and results

3.1. Numerical model

This work analyses output from a three-level nested model described in Paquin et al. (2019). The inner-most component (SJAP100) covers the Saint John Harbour and approach area with 100 m horizontal resolution (Fig. 1a), and is nested within larger regional domains with 500 m and 1/36° horizontal resolutions (Fig. 1b). The model is driven by realistic forcing, which includes atmospheric conditions at the surface, tides and large-scale ocean conditions at the lateral open boundaries, and runoff from the Saint John River.

The nested model is based on version 3.6 of the Nucleus for European Modelling of the Ocean (NEMO) (Madec et al., 2017) without a sea-ice module. It is a z-level model that includes partial cells at the bottom for a more accurate representation of the varying bathymetry, and the "variable volume level" scheme to allow the stretching and compression of the vertical levels according to changes of sea surface elevation. The SJAP100 component has a maximum of 35 levels, with level thickness of about 1 m for the top 20 m of the water column. A partial slip condition is applied along the lateral solid boundaries. The lateral viscosity is proportional to the local shear and tension of the horizontal current (Smagorinsky, 1963). The vertical viscosity is calculated using the κ-ϵ formulation of the general length scale turbulence closure (Umlauf and Burchard, 2003). Bottom friction is parameterized by a quadratic drag law with the background drag coefficient set to 5×10^{-3} for SJAP100, and locally increased to 3×10^{-2} around Reversing Falls for model stability. Evaluation with observational data has shown that SJAP100 possesses high skill in simulating tidal and non-tidal variations in sea level, currents, and stratification in and around Saint John Harbour (Paquin et al., 2019).

In this analysis, we focus on a section of the SJAP100 model domain around Reversing Falls and analyse model output for April 2016, which includes the spring freshet for that year. Fig. 1c shows the model bathymetry in the lower Saint John River. A principal component analysis of depth-averaged velocities in the region bounded by the black box was used to identify the along-channel direction for Reversing Falls; the along-channel section used for analysis follows the orientation of the 1st principal component. The model bathymetry and mean sea surface height linearly interpolated onto the along-channel section are shown in Fig. 3. The boxed region in Fig. 1c was also used to define the background stratification, $\bar{\rho}(z,t)$, at each time step of the hourly model output. In all analyses, compound variables are computed on the NEMO native grid before interpolation onto the along-channel section at approximately 8 m spacing. All form drag and momentum term calculations are computed as integrated values over the segment highlighted in red in Figs. 1c and 3, which starts and ends at the same bathymetric depth.

3.2. Tide propagation over reversing falls

According to the SJAP100 simulation results, the M2 amplitude drops from 0.7 m to 0.3 m and the phase lags by 16° (Fig. 3a) over the 374 m span of Reversing Falls (Fig. 3d). To show the evolution of the sea surface height over a tidal cycle, data were averaged by M2 phase relative to 2016/04/01 00:00:00 UTC in $\pi/12$ increments.

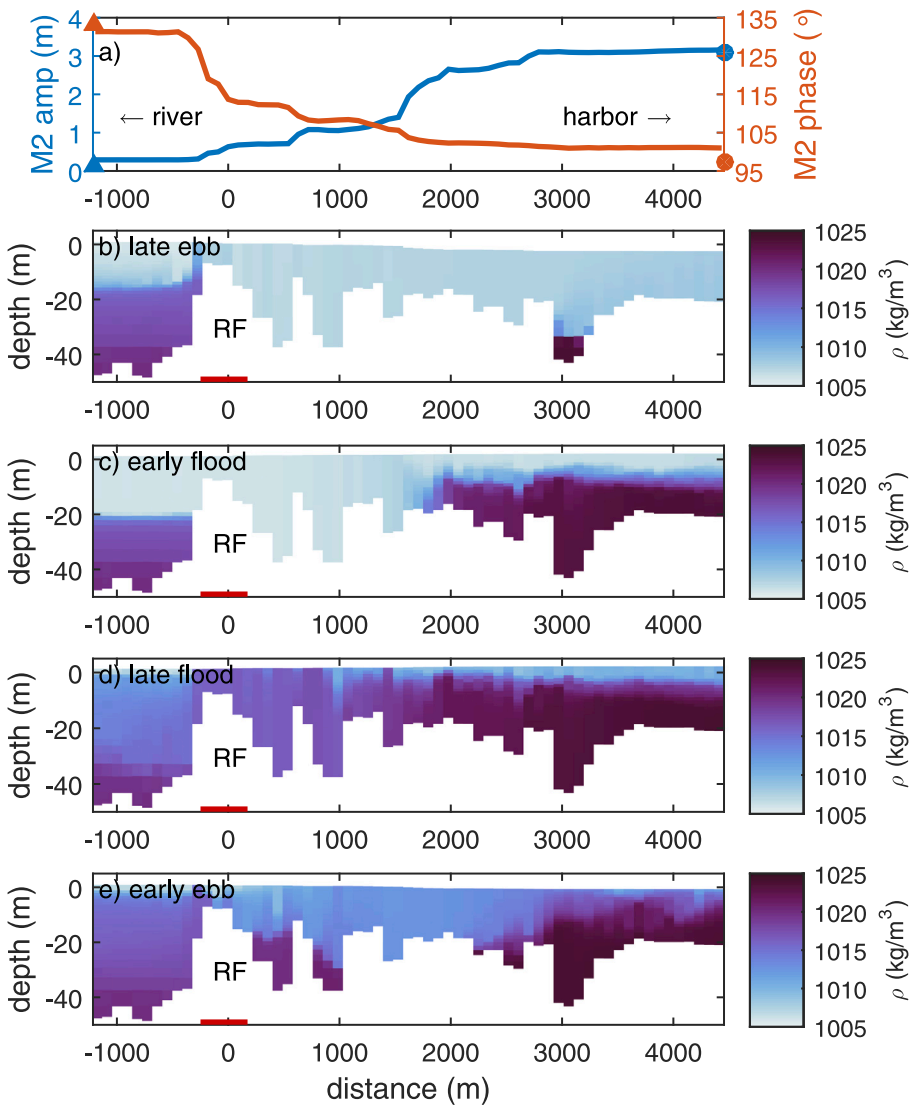

Fig. 4. (a) M2 amplitude and phase over Reversing Falls (RF) and the lower 5 km of the channel. Triangle and circle symbols are data from ECCC and CHS tide gauges indicated on the map in Fig. 1c. (b–e) Density at four tide phases from model grid cells along channel thalweg. Harbour is at the right end of x-axis; upriver direction to the left. Red bar indicates same analysis section highlighted in previous figures. (For interpretation of the references to colour in this figure legend, the reader is referred to the web version of this article.)

The spatial variation in the tidal amplitude and the phase lag over the falls can be seen in the progression of the phase-average sea surface height (Fig. 3b). Upstream water levels never rise as high or fall as low as the downstream extrema, so the flow direction changes when the falling level on the downstream side passes below the level of the upstream side, and when the rising water on the downstream side passes above the level of the upstream side. These transitions occur well after downstream high or low water. For example, the highest two lines in Fig. 3b cross as the water level downstream of the falls drops while the level upstream of the falls rises and the tide still flows upstream. The flow does not change direction until the following phase hour, when the downstream level has fallen below the upstream level.

The tilt of the mean sea surface height (black line in Fig. 3b) depends on the river discharge, which peaked in early April in 2016. The along-channel velocity (Fig. 3c) is positive (ebb direction) for 9.3 h of each tidal cycle. This ebb dominance is partly due to the mean flow of 0.73 m s^{-1} driven by the mean sea surface tilt, which shifts the oscillating velocities towards positive values. However, the along-channel velocity is larger than the mean (black dashed line in Fig. 3c) for 7.7 h of the M2 cycle. This remaining asymmetry is mainly due to the quadratic nature of drag, which limits fast flows more than slow ones and leads to a broad, gradually varying peak in ebb velocities.

Before reaching Reversing Falls, the tide passes over a series of smaller sills in the lower estuary. The M2 tide accumulates a 3 m amplitude reduction and 30° phase lags over the 5 km between Saint John Harbour and Reversing Falls (Fig. 4a). Approaching the river bend 1.5 km southeast of Reversing Falls, the M2 amplitude drops by 1.2 m with a phase lag of just 3°, suggesting some of the tidal signal is reflected back while a portion propagates around the bend. However, field data (Section 4.3) suggests the same phenomenon may not occur in the field. In contrast, at Reversing Falls, there is large phase lag for a relatively smaller drop in amplitude, which is supported by observations (Section 4.3), suggesting that at Reversing Falls, the tide does not propagate like a surface gravity wave.

Two tide gauges are available to compare with the model results: Environment and Climate Change Canada (ECCC) station 01AP005 is above Reversing Falls, and Canadian Hydrographic Service (CHS) station 65 is in the harbour (Fig. 1c). Data from both gauges compare well with the model results (Fig. 4a). When analysed for April 2016, the harbour gauge has an M2 amplitude of 3.07 ± 0.06 m and a phase of $97 \pm 1°$, and the nearest model cell 3.08 ± 0.03 m and $101 \pm 1°$, similar

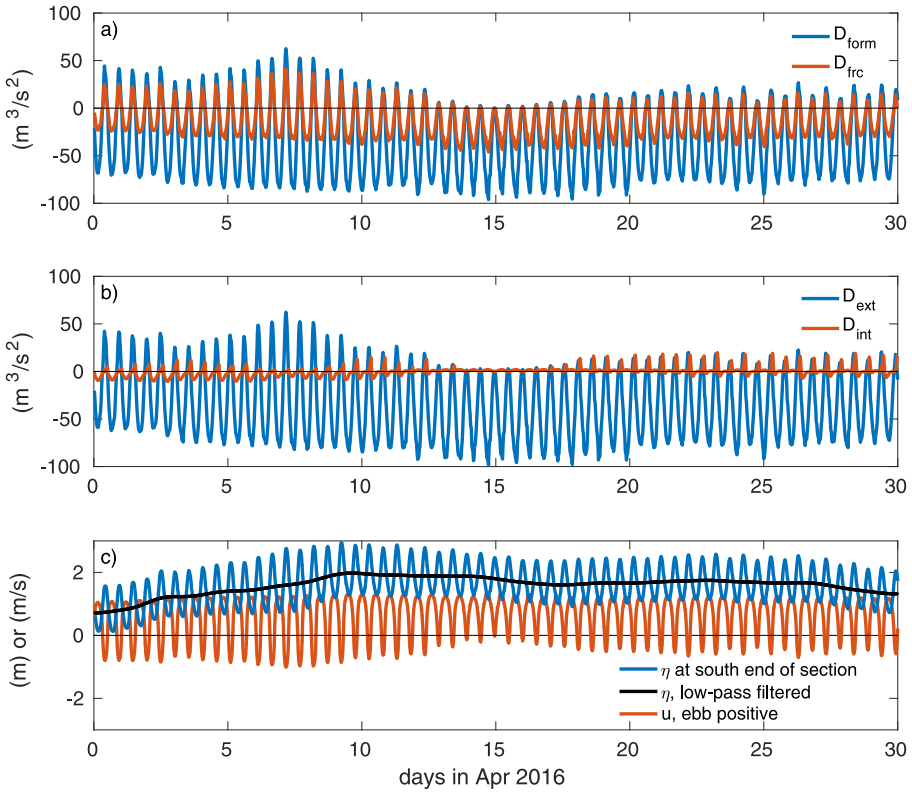

Fig. 5. Drag variables for April 2016. (a) Form and frictional drag over Reversing Falls. (b) External and internal components of form drag over Reversing Falls. (c) Water level, 40-h low-pass filtered water level, and along-channel velocity from the southern end of the Reversing Falls segment.

to the result of Paquin et al. (2019). Above Reversing Falls, gauge data has an M2 amplitude of 0.13 ± 0.004 m and a phase of $133 \pm 2°$, while the nearest model cell has values of 0.27 ± 0.01 m and $134 \pm 1°$.

Depending on tide phase, regions around Reversing Falls can be vertically mixed and salty, vertically mixed and fresh, or highly stratified. There can be up to 10 kg/m^3 difference between similar depths across the falls, and nearly 20 kg/m^3 stratification in 20 m water depth. When the river flow is high in April, most of the lower estuary is flushed with fresh water each ebb tide. Salt remains only where it is trapped behind Revering Falls and in other deep holes in the channel bathymetry (Fig. 4b). During flood tide, stratification is initially advected from the harbour into the river (Fig. 4c). Vertical mixing breaks down the stratification as it passes over sills lower in the estuary, so salt arrives at Reversing Fall abruptly and fully vertically mixed (Fig. 4d). A long ebb tide gradually restratifies Reversing Falls, and then flushes the region downriver of the sill (Fig. 4e, then b).

3.3. Form and frictional drag

Time series of drag variables over Reversing Falls for April 2016 are shown in Fig. 5. Form and frictional drag (Fig. 5a) both always oppose the flow direction (Fig. 5c), but form drag accounts for a majority of the total drag. The average form drag is 2.5 times that of frictional drag, with little variation throughout the tidal cycle (Fig. 6). The ratio of the subtidal components of form and frictional drag (Fig. 7c) peaked at 4.3 on 7 April when spring tide velocities were largest, and was a minimum of 2.1 on 14 April when neap tide velocities were smallest and the high river stage (Fig. 5c) prevented flood direction flows.

The form drag arises from both external and internal pressure anomalies (terms [4] and [5] of Eq. (3)). The external form drag is considerably larger than the internal form drag at Reversing Falls (Fig. 5b). The average magnitude of the internal drag is just 7% of the external drag, and the root mean square value (RMS) is similar, at 9%. However, the ratio of internal to external form drag varies throughout the month and over each tidal cycle. In early April, the internal drag makes a small contribution during both ebb and flood, while in the middle of the month, there is nearly zero internal drag. Towards the end of the month, the internal drag has near zero magnitude on ebb but is similar size to the external drag and slightly phase lagged from it during flood. The varying magnitude of the internal form drag reflects changes in stratification, which could depend on the mixing and advection variation over the spring–neap tidal cycle, and could also depend on the magnitude of the river outflow. The detided and 40-hr low-pass filtered sea surface elevation in Fig. 5c reflects the river stage.

3.4. Momentum balance

The form and frictional drag terms can be compared to other terms in the momentum budget. The momentum terms defined in Eqs. (3) and (4) are shown for a M2 phase-averaged tidal cycle in Fig. 6. These phase-hour data were averaged by M2 phase relative to 2016/04/01 00:00:00 UTC in $\pi/12$ increments. The momentum terms are also shown for one month as the full time series (Fig. 7a) and the detided and 40-hr low-pass filtered component (Fig. 7c).

At both M2 (Fig. 6) and subtidal (Fig. 7c) time scales, the surface pressure gradient is the largest term in the budget, and is primarily balanced by the sum of external form drag, frictional drag, and advection. The barotropic pressure gradient is positive for a ~9 hr ebb tide, and only negative for a ~3 hr flood tide during the average M2 cycle (Fig. 6). Early in the month, when the subtidal surface pressure gradient is smallest (Fig. 7c), the full term (Fig. 7a) alternates between similar size positive (ebb) and negative (flood) peaks. Later in the month when the subtidal pressure gradient is larger, the full term is positive for most of the tidal cycle with brief, smaller negative excursions. The high river discharge in April means the barotropic pressure gradient nearly does not change sign for a few days of neap tides mid-month.

Despite the large vertical and lateral density gradients (Fig. 4) the baroclinic pressure gradient and internal form drag are an order of

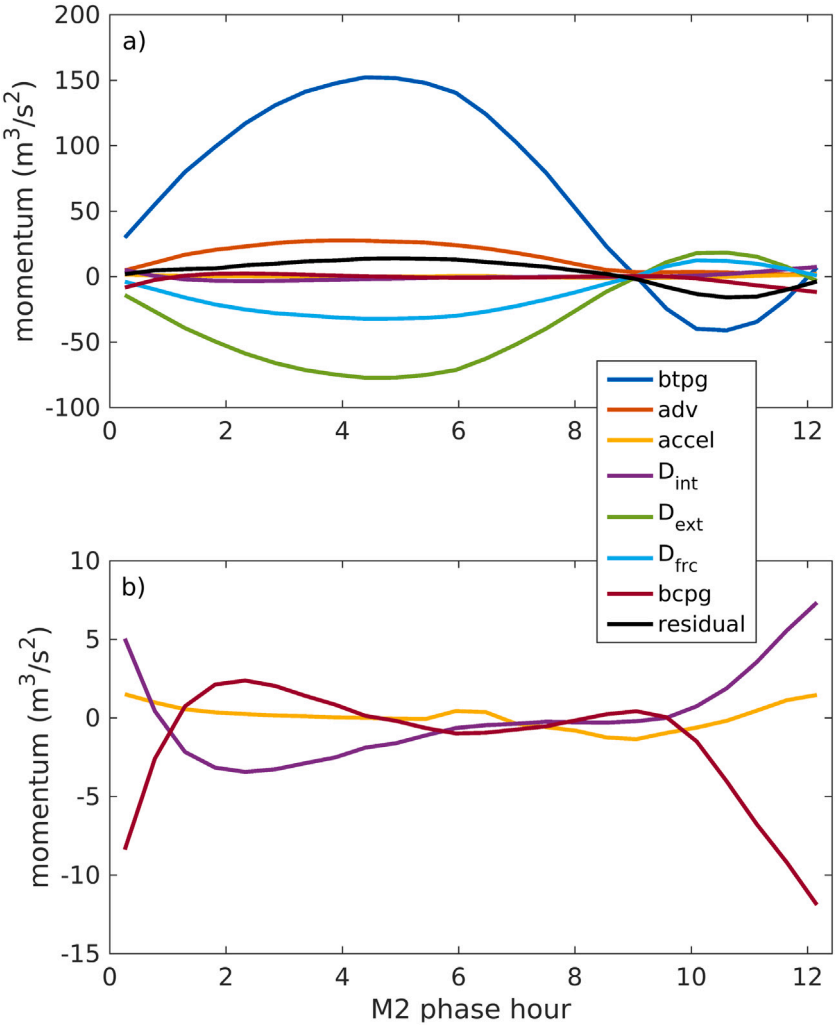

Fig. 6. (a) M2 phase-averaged momentum terms from Eqs. (3) and (4) (b) small terms replotted with tighter *y*-axis limits. Legend abbreviations: btpg is the barotropic pressure gradient; adv is advection; accel is acceleration; D_{int}, D_{ext}, and D_{frc} are the internal, external, and frictional drags; bcpg is the baroclinic pressure gradient.

magnitude smaller than the primary momentum terms in both the tidal and subtidal analyses. These internal terms vary in opposition to each other, with their phase relative to the barotropic tide shifting throughout the month (Fig. 7b). Early in the month, the baroclinic pressure gradient peaks during early ebb and has the same sign as the surface pressure gradient; mid-month, the internal terms are near zero because the region has been flushed with fresh water by the nearly unidirectional flow; late in the month, the baroclinic pressure gradient has large negative peak at high slack as well as a negative peak when the surface pressure gradient is largest at max ebb. The vertical and lateral density gradients driving this internal variation are sensitive to both the river stage and spring–neap cycle. While Reversing Falls certainly affects the stratification of the flow that passes over it, the internal terms of the momentum balance are so much smaller than the external ones that they are unlikely to affect the first order balance under any river flow conditions.

The approximately 2D momentum budget closes to first order (Fig. 8). The mean magnitude of the residual of all momentum terms is 12% of that of the surface pressure gradient, which is the largest term. (RMS is also 12%.) The derivation of the momentum equation (3) made the assumption of 2D flow. However, in the narrow and coarsely resolved model channel, lateral friction may not be negligible. The horizontal viscosity was not saved in the model output, but a rough estimate of lateral mixing based on SJAP100's background horizontal viscosity and lateral shear from model output suggests that including lateral mixing on the right hand side of Eq. (3) could reduce the residual of the momentum terms by approximately 50%. Spatial and temporal variations of lateral circulation around the principal flow direction likely contribute to the remaining residual in the along-channel momentum budget.

The non-wave-like tidal propagation observed over Reversing Falls (Section 3.2) is explained by the relationships between the acceleration and velocity and the surface pressure gradient. In wave propagation, the acceleration is driven by, and therefore proportional to, the surface pressure gradient. At Reversing Falls, this is not the case, as the acceleration is out of phase with the barotropic pressure gradient (Fig. 9a). Instead, the along-channel *velocity* is in phase with the barotropic pressure gradient (it would be out of phase for a wave). The velocity squared is linearly proportional to the pressure gradient (Fig. 9b), indicating that the velocity is set by the instantaneous balance between surface pressure and drag, which scales as u^2. This is a river-like balance that happens to change direction on a tidal period.

4. Discussion

4.1. Comparison to previous work

Reversing Falls differs from a well-studied headland, Three Tree Point in Puget Sound, WA, which has similar tidal amplitude and flow speed. There, Warner et al. (2013) found the surface tilt that drove tidal

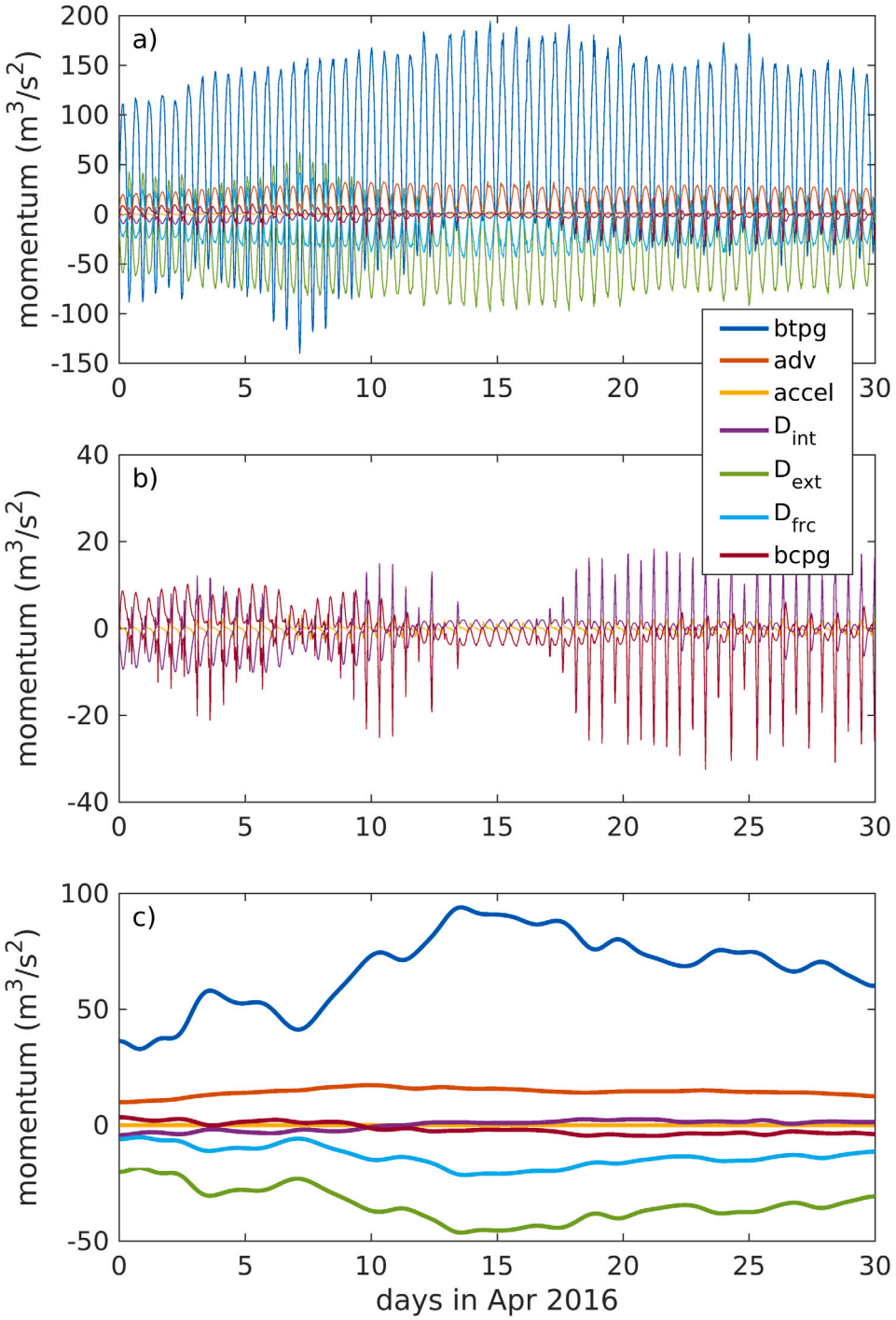

Fig. 7. (a) Momentum terms for April 2016. (b) Small terms replotted with tighter y-axis limits. (c) 40-h low-pass filtered momentum terms. Legend described in Fig. 6 caption.

accelerations also made a significant contribution to form drag. Despite the large tides, at Reversing Falls, acceleration is not a significant term in the momentum balance. Accordingly, there is no form drag contribution owing to the corresponding surface tilt. The Three Tree Point and Reversing Falls sills have similar aspect ratios, but the smaller dimensions of Reversing Falls for the same flow speed means the tidal excursion distance is much longer than Reversing Falls. Warner and MacCready (2009) show that when the tidal excursion distance is much longer than the obstacle length, drag from tide-accelerating tilt is not important. Reversing Falls effectively experiences instantaneously steady flow, even though the tide is, of course, changing over time.

The form drag on Reversing Falls can be used to estimate a bluff body drag coefficient, C_{bb}, for the sill

$$D_{\mathrm{bb}} = 0.5 C_{\mathrm{bb}} u^2 h_o \tag{5}$$

where h_o is the height of the obstacle, taken to be 14.5 m; u is the background flow, taken to be the segment average; and D_{bb} is the drag force per unit width of the channel, taken to be D_{ext}. The regressions shown in Fig. 10 yield C_{bb} of 4.4 and 3.2 on ebb and flood, respectively. While Warner and MacCready (2009) attributed the larger than $O(1)$ bluff body drag coefficients observed at Three Tree Point to the oscillating nature of the flow, it is unclear what causes the large coefficients in the comparatively steady flow at Reversing Falls.

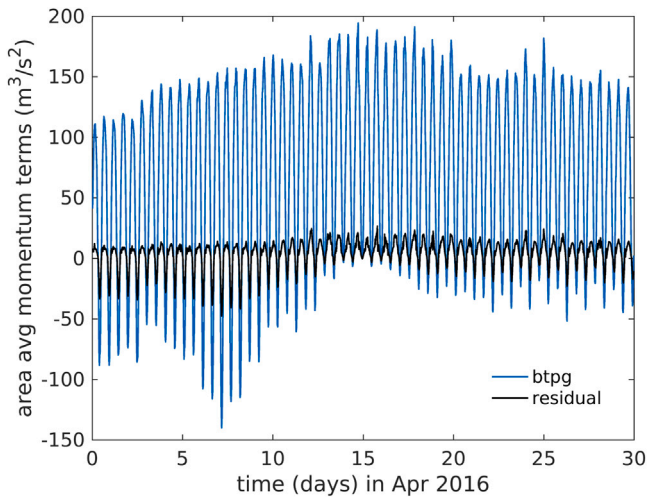

Fig. 8. The surface pressure gradient, which is the largest momentum term from Fig. 7 (blue) and the residual of that term minus all other momentum terms (black). (For interpretation of the references to colour in this figure legend, the reader is referred to the web version of this article.)

4.2. Hydraulic control

In oceanographic contexts, hydraulic control typically refers to flows that are topographically constrained and, near the constriction, are fast enough to limit upstream wave propagation. In these situations, the volume flux depends only on the upstream water depth; for example, weirs are commonly installed in rivers so that discharge can be estimated from depth, which avoids more difficult velocity measurements.

The flow at Reversing Falls is forced over a sill, much like a flow over a river dam, and is also periodically strongly stratified, so both external and internal hydraulic control are potentially important. The external Froude number, $F = \bar{u}/\sqrt{gh}$, is given by the ratio of the depth averaged flow speed to the surface gravity wave speed. Upstream propagating waves are arrested at the critical value of $F = 1$. Atop Reversing Fall, F peaks at approximately 0.35 each ebb tide. Therefore, in this model, the flow passing over the falls is not subject to hydraulic control, such as seen in flows over dams or spillways. In the field, visual inspection of the falls suggests a narrow region in the centre of the river may reach supercritical Froude numbers during ebb tides. The small V-shaped region of smooth surface flow is also visible in some satellite images of the region, but is not resolved in the numerical model.

For two-layer flow, the internal Froude number, G, is given by

$$G^2 = F_1^2 + F_2^2 \qquad \text{where} \tag{6}$$

$$F_1 = \bar{u}_1/\sqrt{g'h_1}, \quad F_2 = \bar{u}_2/\sqrt{g'h_2}, \quad g' = \frac{\Delta\rho}{\rho_o}g \tag{7}$$

where $\bar{u}_i$ and h_i are the velocity and depth within each layer and $\Delta\rho$ is the difference in density between the layers. We use the depth of maximum stratification at each time step to define the boundary between the upper and lower layers. Directly atop Reversing Falls, G is nearly always supercritical, indicating that advection, rather than gravitationally-driven internal wave propagation, moves density fronts over the falls. G is only subcritical for the hour surrounding high slackwater when the barotropic flow pauses and the water column is simultaneously stratified. Just downstream from the falls, deep sections of the channel remain stratified and subcritical for a few hours into ebb tide. This subcritical period allows salt to remain in the lower layer of the water column after the barotropic tide has turned. During April's high river flow, at low slack Reversing Falls has been flushed with fresh water and there is no stratification or meaningful value of G.

4.3. Comparison of model output with field observations from a different year

A field experiment was carried out at Reversing Falls from 23 May to 6 June 2019. Two moorings were deployed, one on each side of Reversing Falls, in quiescent regions to the side of the channel (Fig. 11). Each mooring was anchored by a bottom frame with an RBR*solo*^{3} D pressure sensor that sampled every 0.5 s, and each mooring line held three Sea-Bird SBE37 CTDs, which sampled every 60 s. The upstream mooring was located in 26 m mean water depth (deployment mean of bottom mounted pressure sensor) and the CTDs hung at 2, 5, and 15 m below the surface. The downstream mooring was located in 20 m mean water depth and had CTDs at 2, 5, and 11 m below the surface. The bathymetric depths at the deployment locations are not known accurately relative to the geoid, so only the time-varying components of the RBR pressures are assessed.

These field data were collected during a different year than the one simulated by the model, so comparisons are not intended to be a quantitative model validation. While tidal forcing is consistent year to year, the river flow is not. In an average year, the tide gauge above Reversing Falls (ECCC 01AP005) has a peak maximum daily water level of 3.2 m on May 1. The 2016 model year had a early but typical peak of 3.3 m in early April. In contrast, observations in 2019 occurred following an extreme flood season with a peak over 5.5 m on April 26. Despite these differences, the observations demonstrate the veracity of tidally-varying and along-channel density structure produced by the model.

Variation in density and stratification is sensitive to both river flow and tidal forcing, so we compare the 2019 measured densities to 2016 model output for periods with similar river stage and spring–neap tide phase. The river stage is indicated by the daily-averaged water level at ECCC gauge 01AP005, and the tide phase is indicated by CHS station 65

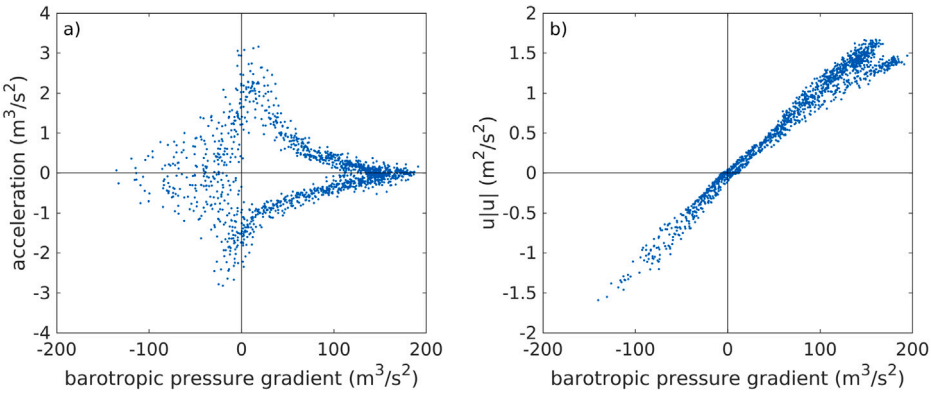

Fig. 9. (a) Acceleration versus the barotropic pressure gradient. (b) Segment-averaged velocity squared versus the barotropic pressure gradient.

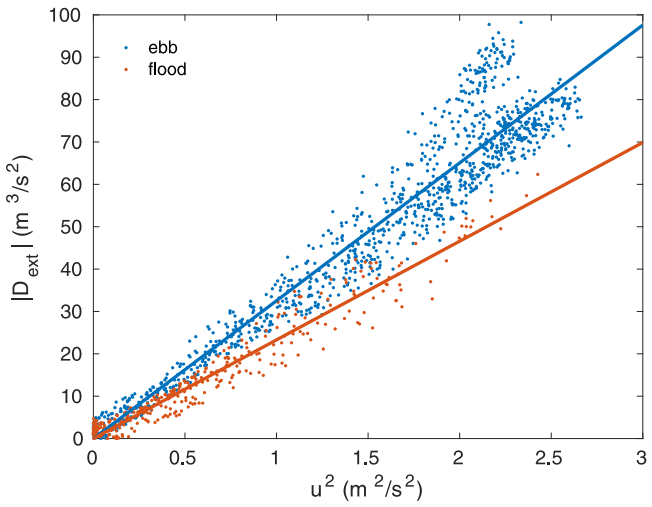

Fig. 10. External form drag versus segment-averaged speed squared, with linear fits used to estimate drag coefficients.

(Fig. 12a, b). CHS chart datum referenced water levels were converted to CGVD28 using a −4.17 m adjustment (CHS via Shannon Nudds, *personal communication*). The 11-day period of 27 April to 7 May 2016 in the model year closely matches the tide and river properties for the 11-day period of 24 May to 3 June 2019 from the field campaign. During both the 2019 field deployment and the 2016 model comparison period, the river level was between 2–3 m and dropping, and the tide progressed from neap to spring.

At the mooring upstream of the falls, model and observations of M2 amplitude are similar (0.30 ± 0.02 m model, 0.24 ± 0.04 m obs, Fig. 13g), and both lag the M2 phase of the downstream mooring by a similar margin (16 ± 5° model, 23 ± 11° obs). Downstream of the falls, the M2 amplitudes are both drastically larger than above the falls (0.68 ± 0.04 m model, 1.86 ± 0.23 m obs, Fig. 13h). However, the modelled M2 is notably smaller than the observed, indicating that the modelled M2 amplitude drop east of the river bend (Section 3.2) is not realistic. This error generated in the narrow but relatively flat river section suggests that the issue is related to lateral or vertical mixing, rather than form drag. Despite the different tidal amplitudes impinging on Reversing Falls, the phase lag over the falls shared between the model and data suggests that the model captures the appropriate flow-restricting dynamics.

Density time series were extracted from the model to match the moored CTD locations and depths. The 11-day comparison period is shown in Fig. 12c–f and a two-day example with measured and modelled densities and surface elevations overlain is shown in Fig. 13. In these data, density is primarily dependent on salinity. At both mooring locations, the near-surface CTD measures the freshest, lightest water and the deepest CTD, the densest. Density peaks at high tide and the peak value is larger for higher harbour tides. The model captures a double-peaked signal at both locations; the second, smaller peak occurs as the ebb velocity increases and causes vertical mixing of deeper, saltier water into the mid and upper water column.

At the upstream site, the modelled and observed surface elevations have similar magnitude and asymmetric shape with a sharper peak and smoother low (Fig. 13g). The model captures the neap to spring increase in the tidal range of density (Fig. 12c, d), from 5 to > 10 kg/m^3 at the deepest CTD and 0 to > 5 kg/m^3 at the top CTD. The model also captures the transition of the middle CTD tracking the top CTD during neap tides and the deeper CTD during spring tides, though this transition happens earlier in the neap–spring transition in the model than in the observations. The timing of the density increase at late flood is consistent between the model and observations, but

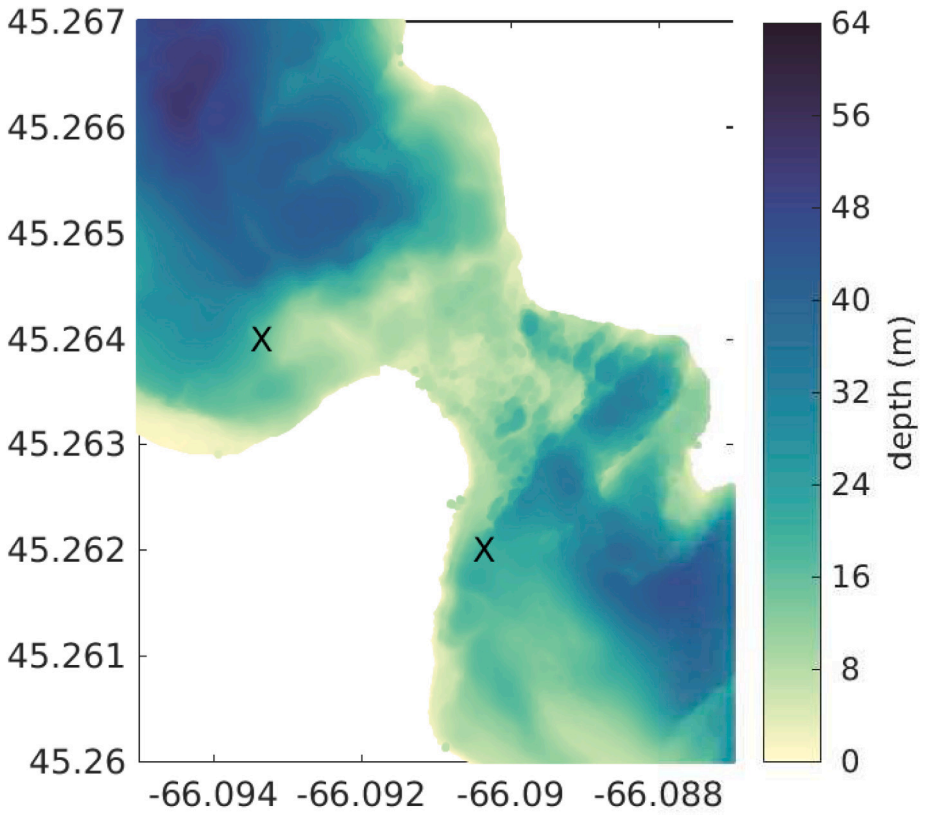

Fig. 11. Field deployment locations for two moorings, each with a bottom pressure sensor, and three CTDs, shown on 1 m resolution surveyed bathymetry provided by Ian Church, UNB.

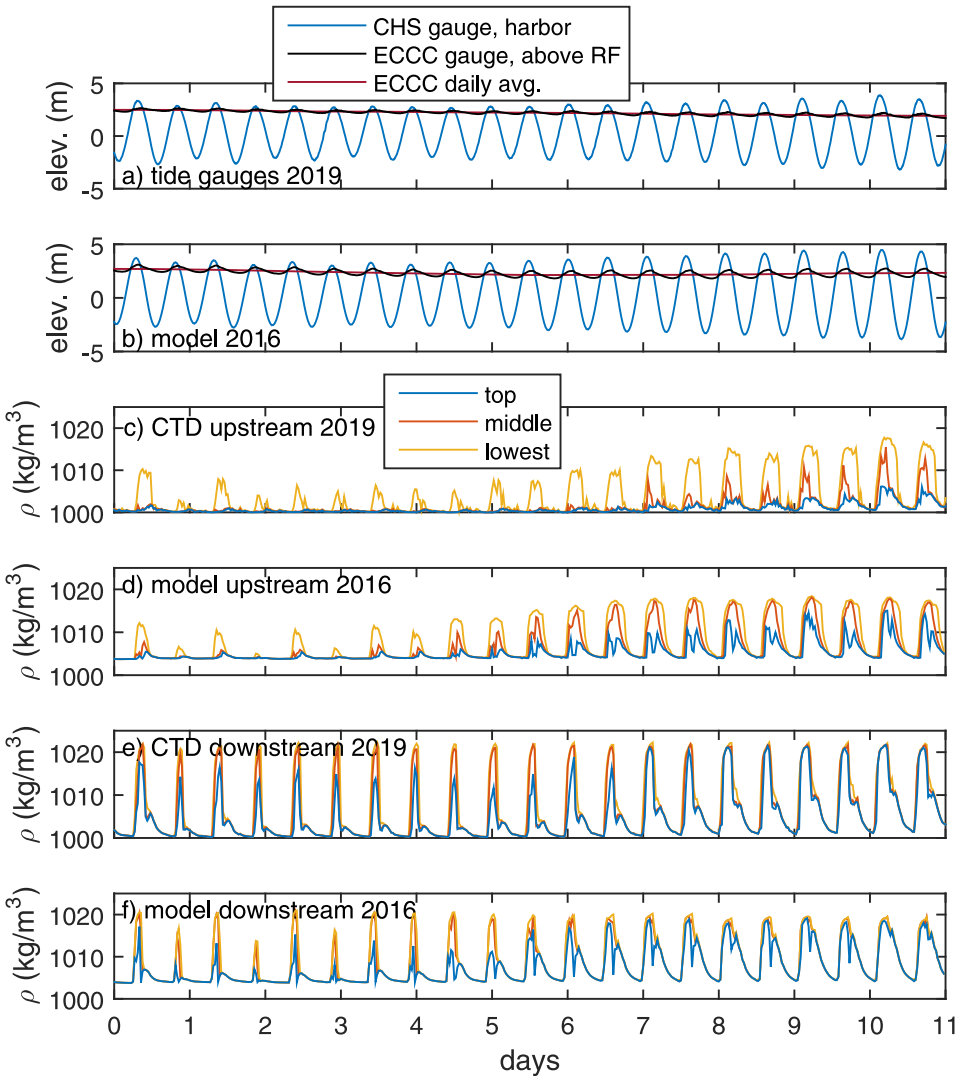

Fig. 12. (a) Water levels from tide gauges shown in Fig. 1c, referenced to CGVD28 for May 24 to June 3 2019, and daily average of ECCC gauge; (b) Model water levels at cells closest to tide gauges from (a), referenced to CGVD28 for April 27 to May 7 2016; (c) Densities from the CTDs on the upstream mooring; (d) Model densities from the upstream mooring location; (e) Densities from the CTDs on the downstream mooring; (f) Model densities from the downstream mooring location. Time referenced to UTC 2019/05/24 00:00 for (a), (c), (e) and UTC 2016/04/27 00:00 for (b), (d), (f). CTD data are sub-sampled on a 30 min interval to match model output interval.

the elevated density persists longer into ebb in the model than the observations (Fig. 13a, c, e). More vertical mixing and less freshwater preconditioning in the model than in the observations may contribute to these differences in stratification.

At the downstream site (Fig. 12e, f, Fig. 13b, d, f), the tidal variation of density is larger, 20 kg/m^3, in the observations and 15 kg/m^3 in the model, at the deepest CTD. The smaller density range in the model may be due to the smaller tidal amplitude that impinges on Reversing Falls (Fig. 13h) leading to a smaller tidal excursion. Density at the middle CTD tracks closely with the deeper one, and the top CTD measures density peaks approximately 5–10 kg/m^3 lighter during neap tides, and similar to the deeper CTDs during spring tides. The modelled and observed densities follow the same asymmetric shape of a fast rise and slower decrease. The rapid increase occurs during late flood when a salinity front is advected up over the falls.

Despite model and observation being from different years, the model clearly tracks the observed shape of the tidal cycle of density at each depth at each site in Fig. 13, indicating the primary along-channel baroclinic dynamics are the same. At both sites, the lowest density in each tidal cycle is near 1000 kg/m^3 in the observations and 1005 kg/m^3 in the model. This difference is expected because 2019 had extremely high river flows for the month prior the field observations, which preconditioned the region to have lower salinities than in the more typical 2016.

4.4. Model limitations

While the model resolution in the river is not sufficient to capture lateral features, such as the baroclinic secondary (cross-channel) circulation, the close match of the modelled to measured vertical and along-channel density structure indicates the along-channel baroclinic response of the model is realistic at the resolved scales. The lateral resolution limits the sharpness of tidal fronts, and therefore the instantaneous strength of baroclinic forcing. Therefore, baroclinic terms may be larger than those shown in Section 3.4, particularly during brief periods in each tidal cycle when the tidal front is advected over Reversing Falls.

This model cannot resolve the small scale eddies that are prevalent at the study site. Visual inspection of the field site indicates that the flow over Reversing Falls is relatively symmetric around the centre line of the flow, and that the direction of the mean flow advecting the small scale eddies is laterally uniform for several hundred metres downstream of the falls. We aim to describe the processes acting on scales resolved by the model, but acknowledge that a higher resolution model may

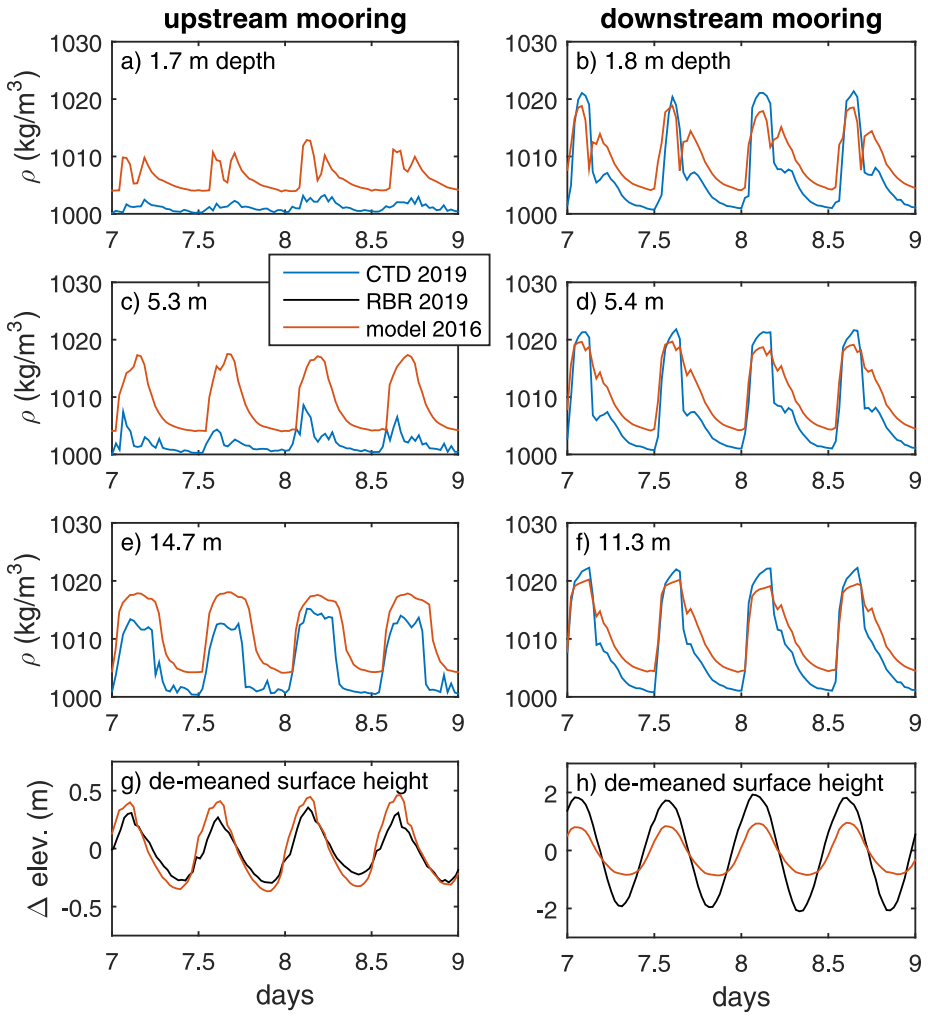

Fig. 13. (a–f) Density at three depths and (g, h) the time-varying component of surface elevation from upstream (left) and downstream (right) of Reversing Falls, from 2019 field measurements and 2016 model output for two days with similar river levels and tide phases. The mean over the two-day window shown has been subtracted from the elevation data. Time reference and data interval same as in Fig. 12.

have a significant contribution from lateral mixing and stirring, and produce a laterally inhomogeneous flow.

A 2D barotropic nonhydrostatic model of the region successfully carries a large (2.1 m) M2 amplitude to the base of Reversing Falls (David Greenberg, *unpublished*). The model's unstructured grid, based on WebTide (Dupont et al., 2005) and substantially refined near the port of Saint John, NB, has approximately 10 m horizontal resolution near Reversing Falls and 30 m resolution in the river downstream of the falls. However, this 2D model propagates three times the observed M2 amplitude (0.74 m) to the upstream side of the falls. A 2D model cannot simulate laterally overturning, helical cells that could develop owing to curvature of the channel; the absence of these in the 2D model could contribute to it carrying too much momentum up over the falls. In both the 2D model and in SJAP100, the external form drag balances roughly half the barotropic pressure gradient, suggesting that the form drag is insensitive to resolution as long as the total relief in the bathymetry is consistent. In the 2D model, depth-average velocities are twice as large as in SJAP100, advection is leading order, and frictional drag ($C_d = 2.2\times10^{-3}$) is negligible. As with the velocities, the peak Froude number was double that of SJAP100, approximately 0.8. These results indicate that resolution finer than 10 m may be needed to produce the supercritical flow region informally observed in the centre of the channel. A baroclinic, nonhydrostatic model would be required to assess internal supercritical features such as internal hydraulic jumps or solitary waves. The veracity of the density structure generated by our 3D model indicates that even if the parameterized mixing has compensated for unresolved internal nonhydrostatic processes, the resulting internal pressure gradient is small compared to the external field. Therefore, internal processes are unlikely to be a primary energy sink limiting barotropic tidal propagation upstream.

Our model underestimates the tidal amplitude impinging on Reversing Falls owing to too much damping in the lower stretch of the river (Fig. 13h). We expect this is the main contributing factor to our likely underestimate of max speed over Reversing Falls, and resulting low Froude number. Additionally, our present model can only simulate the 100 m spatial average of the currents, so if the fastest flow is limited to less than 100 m of cross- or along-channel area, our model will also underestimate the maximum Froude number relative to the study site.

5. Summary

In this work, we determined the relative importance of form and frictional drag at impeding flow over Reversing Falls, a sill in the Saint John River estuary, and assessed the dynamical control of the M2 tide phase lag over the sill. Over Reversing Falls, form drag is two and a half times the size of frictional drag, so it is primarily responsible for slowing both the ebb and flood tidal currents. This form drag is almost entirely external, arising from sea surface height anomalies rather than internal density anomalies, despite large variation in vertical and horizontal density gradients over each tidal cycle.

The leading order momentum balance is of form and frictional drag opposing the barotropic pressure gradient. This steady balance reflects river-like dynamics of a gravitationally driven flow that would accelerate until quadratic drag became large enough to balance the pressure gradient from surface tilt. Reversing Falls has the peculiarity that the terms in this steady balance change sign about four times a day.

In our model, the M2 tide amplitude drops by 0.4 m and phase lags by 16° in the few hundred metres over the falls. This phase lag is large relative to the amplitude drop when compared to the 17° phase lag and 2.4 m amplitude drop that is incurred over a 4 km stretch with a more gradually varying bathymetry between the harbour and the falls. The steady dynamical balance demonstrates that at Reversing Falls the tide is not propagating like a surface gravity wave with energy loss. Rather, the water moves over the sill in proportion to the (square root of) the pressure gradient, and flow direction switches when the down-river side of the falls passes the height of the up-river side.

These model results are supported by available field observations of water levels and densities, which show similar M2 amplitude and phase lag, and tidally-varying stratification to the modelled values. The model reproduces the M2 phase lag and amplitude drop between tide gauges 1 km upstream and 5 km downstream from the falls, which suggests that the model captures appropriate flow-restricting dynamics on a large scale. Nearby moored measurements from a different year than the model experiment demonstrate that the model captures the time- and depth-varying density structure of the tidal front. The accompanying pressure measurements demonstrated the phase lag induced immediately over Reversing Falls is reasonable, but also revealed the shortcoming that too little M2 amplitude passes up the narrow river to impinge on Reversing Falls. The accuracy of the tide propagation in the model lends confidence to the fidelity of the model's driving dynamics. However, further observations in the fast flow region immediately around Reversing Falls are needed to fully validate the model results, and the horizontal resolution of the model also needs to be increased to better resolve internal and lateral gradients over such steep bathymetry. Though this model is an imperfect representation of the real river, the main conclusion from our analysis, that form rather than frictional drag is the major force impeding tidal propagation over the falls, appears robust despite the model's shortcomings.

Declaration of competing interest

The authors declare that they have no known competing financial interests or personal relationships that could have appeared to influence the work reported in this paper.

Acknowledgements

We thank Clark Richards for the loan of pressure sensors, and we thank Ian Church for providing high resolution bathymetry for the Reversing Falls region. We also thank the captain and crew of the CCGS Viola M. Davidson, and D.M.K. Marine Services Ltd. for their deployment and recovery of field equipment. We thank Alex Hay and Sally Warner for their help in understanding the background material on which this work was based. We thank the anonymous reviewers whose comments have greatly improved this manuscript.

This study is supported by the Oceans Protection Plan and the Government of Canada.

References

Church, I., 2014. Modelling the Estuarine Circulation of the Port of Saint John: Applications in Hydrographic Surveying (Ph.D. thesis). The University of New Brunswick.

Dupont, F., Hannah, C.G., Greenberg, D., 2005. Modelling the sea level of the upper bay of fundy. Atmos.-Ocean 43 (1), 33–47, https://doi.org/10.3137/ao.430103.

Edwards, K.A., MacCready, P., Moum, J.N., Pawlak, G., Klymak, J.M., Perlin, A., 2004. Form drag and mixing due to tidal flow past a sharp point. J. Phys. Oceanogr. 34 (6), 1297–1312. http://dx.doi.org/10.1175/1520-0485(2004)034<1297:FDAMDT>2.0.CO;2.

Friedrichs, C.T., Aubrey, D.G., 1988. Non-linear tidal distortion in shallow well-mixed estuaries: a synthesis. Estuar. Coast. Shelf Sci. 27 (5), 521–545. http://dx.doi.org/10.1016/0272-7714(88)90082-0.

Gille, S.T., 1995. Dynamics of the Antarctic Circumpolar Current. Evidence for Topographic Effects from Altimeter Data and Numerical Model Output (Ph.D. thesis). Massachusetts Institute of Technology, https://apps.dtic.mil/dtic/tr/fulltext/u2/a305871.pdf.

Godin, G., 1985. Modification of river tides by the discharge. J. Waterw. Port Coast. Ocean Eng. 111 (2), 257–274. http://dx.doi.org/10.1061/(ASCE)0733-950X(1985)111:2(257).

Godin, G., 1991. Tidal hydraulics of Saint John River. J. Waterw. Port Coast. Ocean Eng. 117 (1), 19–28. http://dx.doi.org/10.1061/(ASCE)0733-950X(1991)117:1(19).

Johnson, G.C., Bryden, H.L., 1989. On the size of the antarctic circumpolar current. Deep-Sea Res. A 36 (1), 39–53. http://dx.doi.org/10.1016/0198-0149(89)90017-4.

Kundu, P.K., 2012. Fluid Mechanics, Fifth ed. Academic Press, Boston, pp. 361–419. http://dx.doi.org/10.1016/B978-0-12-382100-3.10009-5.

Leys, V., 2007. 3D flow and sediment transport modelling at the reversing falls - Saint John Harbour, New Brunswick. In: OCEANS 2007, pp. 1–16. http://dx.doi.org/10.1109/OCEANS.2007.4449139.

MacCready, P., Pawlak, G., Edwards, K., McCabe, R., 2003. Form drag on ocean flows. In: Proceedings of the 13th "Aha Huliko"a Hawaiian Winter Workshop: Near-Boundary Processes and their Parameterization. pp. 119–130, http://www.soest.hawaii.edu/PubServices/2003pdfs/MacCready.pdf.

Madec, G., Bourdallé-Badie, R., Bouttier, P.-A., Bricaud, C., Bruciaferri, D., Calvert, D., Chanut, J., Clementi, E., Coward, A., Delrosso, D., Ethé, C., Flavoni, S., Graham, T., Harle, J., Iovino, D., Lea, D., Lévy, C., Lovato, T., Martin, N., Masson, S., Mocavero, S., Paul, J., Rousset, C., Storkey, D., Storto, A., Vancoppenolle, M., 2017. NEMO Ocean Engine (Version v3.6). Zenodo, https://doi.org/10.5281/zenodo.1472492.

Metcalfe, C.D., Dadswell, M.J., Gillis, G.F., Thomas, M.L.H., 1976. Physical, Chemical, and Biological Parameters of the Saint John River Estuary, New Brunswick, Canada. Fisheries and Marine Service Technical Report 686, Environment Canada.

Moum, J.N., Nash, J.D., 2000. Topographically induced drag and mixing at a small bank on the continental shelf. J. Phys. Oceanogr. 30 (8), 2049–2054. http://dx.doi.org/10.1175/1520-0485(2000)030<2049:TIDAMA>2.0.CO;2.

Nash, J.D., Moum, J.N., 2001. Internal hydraulic flows on the continental shelf: High drag states over a small bank. J. Geophys. Res. 106 (C3), 4593–4611, https://agupubs.onlinelibrary.wiley.com/doi/abs/10.1029/1999JC000183.

Paquin, J.-P., Lu, Y., Taylor, S., Blanken, H., Marcotte, G., Hu, X., Zhai, L., Higginson, S., Nudds, S., Chanut, J., Smith, G.C., Bernier, N., Dupont, F., 2019. High-resolution modelling of a coastal harbour in the presence of strong tides and significant river runoff. Ocean Dyn. https://doi.org/10.1007/s10236-019-01334-7.

Parker, B.B., 1991. Chapter: The relative importance of the various nonlinear mechanisms in a wide range of tidal interactions. In: Tidal Hydrodynamics. John Wiley and Sons, pp. 237–268.

Prandle, D., 1991. Chapter: Tides in estuaries and embayments. In: Tidal Hydrodynamics. John Wiley and Sons, pp. 125–152.

Pratt, L.J., Whitehead, J.A., 2008. Rotating Hydraulics: Nonlinear Topographic Effects in the Ocean and Atmosphere. Springer.

Sankaranarayanan, S., McCay, D.F., 2003. Three-dimensional modeling of tidal circulation in bay of fundy. J. Waterw. Port Coast. Ocean. Eng. http://dx.doi.org/10.1061/(ASCE)0733-950X(2003)129:3(114).

Smagorinsky, J., 1963. General circulation experiments with the primitive equations. Mon. Weather Rev. 91 (3), 99–164. http://dx.doi.org/10.1175/1520-0493(1963)091<0099:GCEWTP>2.3.CO;2.

Speer, P., Aubrey, D., 1985. A study of non-linear tidal propagation in shallow inlet/estuarine systems Part II: Theory. Estuar. Coast. Shelf Sci. 21 (2), 207–224. http://dx.doi.org/10.1016/0272-7714(85)90097-6.

Trites, R.W., 1960. An oceanographical and biological reconnaissance of kennebecasis bay and the Saint John River Estuary. J. Fish. Res. Board Can. 17 (3), 377–408, https://doi.org/10.1139/f60-029.

Umlauf, L., Burchard, H., 2003. A generic length-scale equation for geophysical turbulence models. J. Mar. Res. 61 (2), 235–265. http://dx.doi.org/10.1357/002224003322005087.

Warner, S.J., MacCready, P., 2009. Dissecting the pressure field in tidal flow past a headland: When is form drag "real"? J. Phys. Oceanogr. 39 (11), 2971–2984, https://doi.org/10.1175/2009JPO4173.1.

Warner, S.J., MacCready, P., Moum, J.N., Nash, J.D., 2013. Measurement of tidal form drag using seafloor pressure sensors. J. Phys. Oceanogr. 43 (6), 1150–1172, https://doi.org/10.1175/JPO-D-12-0163.1.